Unconventional skyrmions in an interfacial frustrated triangular lattice

Arnob Mukherjee [1,*] Amit B. Sanyal,[1] and Elbio Dagotto[1,2]

[1]*Department of Physics and Astronomy, The University of Tennessee, Knoxville, Tennessee 37996, USA*
[2]*Materials Science and Technology Division, Oak Ridge National Laboratory, Oak Ridge, Tennessee 37831, USA*

Magnetic skyrmions are spin topological textures of potential interest in spintronics-related data storage and processing devices. Here, we show the emergence of unconventional skyrmions in a geometrically frustrated triangular lattice on an inversion-symmetry-breaking two-dimensional electron gas substrate. Starting with a classical double-exchange mechanism, this generic interface induces exotic skyrmionic and unique noncoplanar magnetic states not observed in the equivalent square lattice interface. We study the model by deriving an effective spin Hamiltonian. Large scale classical Monte Carlo simulations provide a quantitative evidence for the emergence of these exotic magnetic states. We found that these chiral magnetic states exhibit a substantial and nonzero topological Hall conductivity. As potential material candidates, we propose Cr/MoS_2, Fe/MoS_2, and Fe/WSe_2 interfaces because they have the requisite underlying triangular lattice structures and large spin-orbit coupling.

I. INTRODUCTION

Chiral magnetism has drawn much attention in the scientific community due to its potential applications in spintronics devices and its role in achieving enhanced topological Hall response. A dominant example of such chiral magnetic texture with an intrinsic topological nature is a skyrmion [1–12]. In metallic interfaces [13–16], the existence of such skyrmion textures makes it possible to manipulate them with very ultralow currents, and the topological protection [17–22] makes them a robust buildingblock for next-generation technological applications. Additionally, the presence of these exotic noncoplanar magnetic configurations in metals can improve the spin-polarized charge transport [23,24]. Our findings open new avenues and have important implications for the development of advanced spintronics devices and nanoelectronics.

These topologically protected spin structures exhibit ultralow current density dynamics and large Hall currents, making them attractive for technological applications. However, the skyrmion Hall effect, which results in the transverse deflection of skyrmions under the application of an electric current [25–27], represents a significant hurdle to the practical implementation of skyrmion-based devices. To overcome this limitation, various strategies have been proposed. Recent studies have explored addressing the challenge of the skyrmion Hall effect by coupling merons with opposite topological charges [28]. Another promising approach being the manipulation of the nature of the skyrmion state in such a manner that the Magnus force cancels out [29–31]. This has led to the emergence of unconventional skyrmion textures, such as antiferromagnetic skyrmion, skyrmionium, mixed skyrmions, etc. [32–39], as potential alternatives. They retain the fa-

vorable properties of traditional skyrmions while minimizing the skyrmion Hall effect. These findings have important implications for the continued development of skyrmion-based technologies.

In this work, we present a unique mechanism for the generation of unconventional magnetic states through the manipulation of frustration in interfacial triangular systems. By tuning the antiferromagnetic exchange interactions in the upper insulating layer, we induce frustration, leading to the emergence of magnetic states with unique properties at the interface between the insulator and a spin-orbit coupled two-dimensional electron gas (2DEG). This approach opens up a new avenue for the manipulation of magnetic properties at the nanoscale and holds the potential for the development of advanced spintronics and data storage devices. The findings of this study are potentially significant in condensed matter physics and may have implications for the advancement of various technologies.

II. MODEL

We start with a bilayer system with the upper layer having an antiferromagnet insulator on top of a spin-orbit coupled metal. A generic electronic Hamiltonian for such bilayers is given by

$$
\begin{aligned}
H = &-t_\gamma \sum_{i,\gamma,\sigma} (c_{i,\sigma}^\dagger c_{i+\gamma,\sigma} + \text{H.c.}) \\
&- i\lambda \sum_{i,\gamma,\sigma\sigma'} c_{i\sigma}^\dagger [\hat{z} \cdot (\boldsymbol{\tau} \times \hat{\gamma})]_{\sigma\sigma'} c_{j\sigma'} \\
&- J_{\text{H}} \sum_i \mathbf{S}_i \cdot \boldsymbol{\tau}_i + J_{\text{AF}} \sum_{\langle ij \rangle} \mathbf{S}_i \cdot \mathbf{S}_j - h_z \sum_i S_i^z. \quad (1)
\end{aligned}
$$

*arnobmukherjee1988@gmail.com

The operator $c_{i\sigma}^{\dagger}$ ($c_{i\sigma}$) creates (annihilates) an electron at site i with spin $\sigma \in \{\uparrow, \downarrow\}$. The first term represents the electronic kinetic energy of the nearest neighbor (nn) hopping t_γ from the site i to site $j = i + \gamma$. The basic energy scale here is set by $|t_\gamma| = 1$, which is γ independent. Assuming the lattice constant to be unity, $\hat{\gamma} \in \{\mathbf{a}_1, \mathbf{a}_2, \mathbf{a}_3\}$ denotes the basis unit vector of the triangular Bravais lattice with $\mathbf{a}_1 = (1, 0)$, $\mathbf{a}_2 = (1/2, \sqrt{3}/2)$, and $\mathbf{a}_3 = (-1/2, \sqrt{3}/2)$. The second term is the Rashba spin-orbit coupling of strength λ, generated via interfacial inversion symmetry breaking. $\boldsymbol{\tau}$ is a vector operator with the three Pauli matrices as components. $\mathbf{S}_i$ denotes the localized spins, which we assume to be classical vectors with magnitude $|\mathbf{S}_i| \equiv 1$. $\mathbf{s}_i$ is the electronic spin operator, given by $\mathbf{s}_i = (1/2) \sum_{\sigma,\sigma'} c_{i\sigma}^{\dagger} \boldsymbol{\tau}_{\sigma\sigma'} c_{i\sigma'}$. The third term represents the interlayer ferromagnetic Hund's coupling J_{H}, where the magnetic moments of the insulating layer influence on the conduction electrons and vice versa. The last two terms represent the intralayer antiferromagnetic exchange (J_{AF}) and a magnetic Zeeman field (h_z) applied along the z axis.

We emphasize that the interfacial frustrated system presented in this effort has been successfully implemented experimentally [40–44]. In previous studies, analogous interface engineering approaches have been utilized to explore the topological Hall effect present in chiral magnetic materials. The empirical realization of these interfacial systems further underscores the significance and impact of our current study. Furthermore, antiferromagnetic skyrmions have been stabilized by coupling a bipartite skyrmion material to a collinear antiferromagnetic layer [45]. In the presence of this antiferromagnetic layer, the skyrmions on one sublattice experience an effective staggered magnetic field, which leads to the flip of spins of the same sublattice. This proposed model was based solely on classical spins and thus applicable only to insulators. In contrast, the present study considers the impact of itinerant electrons and geometric frustration, and the mechanism is relevant to metals with spin-orbit coupling.

When there is a significant proximity effect, the interaction between localized spins in the magnetic layer and electronic spins can be considered substantial. Under these conditions, the double exchange approximation ($J_{\mathrm{H}} \to \infty$) serves as the conventional analytical framework. By considering the large J_{H} limit, the Rashba double-exchange (RDE) Hamiltonian [46] can be derived as,

$$H_{\mathrm{RDE}} = \sum_{\langle ij \rangle, \gamma} \left[g_{ij}^{\gamma} d_i^{\dagger} d_j + \mathrm{H.c.} \right] + J_{\mathrm{AF}} \sum_{\langle ij \rangle} \mathbf{S}_i \cdot \mathbf{S}_j - h_z \sum_i S_i^z, \tag{2}$$

where d_i ($d_i^{\dagger}$) annihilates (creates) an electron at site i with spin parallel to the localized spin. The Zeeman coupling of spins to an external magnetic field of strength h_z has been included as the last term in Eq. (2). The projected hopping $g_{ij}^{\gamma} = t_{ij}^{\gamma} + \lambda_{ij}^{\gamma}$ depends on the orientations of the local moments $\mathbf{S}_i$ and $\mathbf{S}_j$ [46,47]. A recent investigation has led to the derivation of an effective spin model by integrating out the electrons from the Rashba double-exchange Hamiltonian [Eq. (2)]. The resulting effective model can be expressed as

follows:

$$H_{\mathrm{eff}} = -\sum_{\langle ij \rangle} D_{ij}^{\gamma} f_{ij}^{\gamma} + J_{\mathrm{AF}} \sum_{\langle ij \rangle} \mathbf{S}_i \cdot \mathbf{S}_j - h_z \sum_i S_i^z,$$

$$f_{ij}^{\gamma} = 1/\sqrt{2}[t^2(1 + \mathbf{S}_i \cdot \mathbf{S}_j) + 2t\lambda \hat{\gamma}' \cdot (\mathbf{S}_i \times \mathbf{S}_j)$$
$$+ \lambda^2 \{1 - \mathbf{S}_i \cdot \mathbf{S}_j + 2(\hat{\gamma}' \cdot \mathbf{S}_i)(\hat{\gamma}' \cdot \mathbf{S}_j)\}]^{1/2},$$

$$D_{ij}^{\gamma} = \left\langle \left(e^{ih_{ij}^{\gamma}} d_i^{\dagger} d_j + \mathrm{H.c.} \right) \right\rangle_{gs}, \tag{3}$$

where we use the expression $\hat{\gamma}' = \hat{z} \times \hat{\gamma}$, $f_{ij}^{\gamma}(h_{ij}^{\gamma})$ represents the modulus and argument of the complex number g_{ij}^{γ}, and $\langle \hat{O} \rangle_{gs}$ represents the expectation values of the operator $\hat{O}$ in the ground state. The Hamiltonian Eq. (3) can be effectively represented using a constant value for D_{ij}^{γ}, and in this case, D_{ij}^{γ} is set to $D_{ij}^{\gamma} \equiv D_0 = 1$ for our simulations [47]. It is worth noting that the effective spin model has an identical functional form when derived from a simple two-site picture [17]. The results discussed in the following sections are obtained with λ set to 0.4. Our prior research established the stabilization of the fDW state at $\lambda = 0.4$ and $h_z = 0.0$, which is experimentally known to precede the SkX phase [12]. Consequently, we target this fDW phase at $\lambda = 0.4$ in the present study to explore the emergence of unconventional magnetism. We simulate H_{eff} [Eq. (3)] using the classical Monte Carlo approach based on the Metropolis algorithm. Please see Appendix A] for details on simulation technique. The presence of topological magnetic phases is inferred via the local skyrmion density $\mathcal{T}$ [35,39]

$$\mathcal{T} = \frac{1}{4\pi} \left[\sum_i A_i^{(12)} \mathrm{sgn}\left[\mathcal{L}_i^{(12)} \right] + A_i^{(45)} \mathrm{sgn}\left[\mathcal{L}_i^{(45)} \right] \right],$$

$$\mathcal{L} = \frac{1}{8\pi} \left\langle \sum_i \mathcal{L}_i^{(12)} + \mathcal{L}_i^{(45)} \right\rangle, \tag{4}$$

where $A_i^{(ab)} = ||(\mathbf{S}_{i_a} - \mathbf{S}_i) \times (\mathbf{S}_{i_b} - \mathbf{S}_i)||/2$ is the local area of the surface spanned by three spins on every elementary triangular plaquette $\mathbf{r}_i, \mathbf{r}_a, \mathbf{r}_b$. Here $\mathcal{L}_i^{(ab)} = \mathbf{S}_i \cdot (\mathbf{S}_{i_a} \times \mathbf{S}_{i_b})$ is the local chirality and $\mathbf{r}_i, \mathbf{r}_1 - \mathbf{r}_5$ are the sites involved in the calculation of $\langle \mathcal{T} \rangle$ [39].

III. PHASE DIAGRAM

In Refs. [47,48], the $J_{\mathrm{AF}} = 0$ limit of the model was explored on chiral metallic systems with a square lattice as an underlying geometry, revealing a stable state of filamentary domain wall (fDW) structures at low temperatures and small λ and h_z values. With increasing magnetic field, the system transitions to a skyrmionic crystal (SkX) and skyrmion gas (SkG) states before eventually reaching the saturated ferromagnetic (FM) state. The phase diagram in the h_z-J_{AF} plane, depicted in Fig. 1, summarizes the impact of AFM exchange coupling on the localized spins of the triangular lattice at low temperatures. The phase diagram includes topologically trivial states, such as the single-Q (SQ) spiral and the saturated ferromagnetic (FM), as well as more exotic states like the filamentary domain wall (fDW), skyrmion crystal (SkX), skyrmion gas (SkG), bimeron-skyrmion (BM-Sk), mixed skyrmion (MSk), vortex (VX), mixed state 2 (MX), noncoplanar (NCP), and an
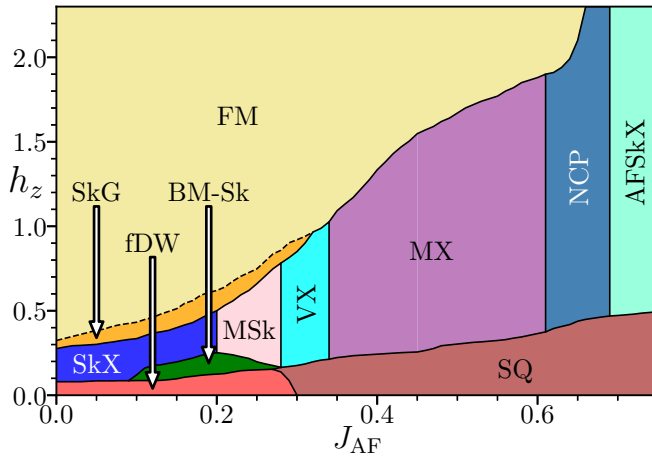
FIG. 1. The phase diagram in the h_z vs J_{AF} plane at low temperature ($T = 0.001$) for an interfacial frustrated triangular system. It reveals the presence of several exotic magnetic phases in addition to the expected saturated ferromagnetic (FM) and single-Q spiral states (SQ). These include filamentary domain wall (fDW), skyrmion crystal (SkX), skyrmion gas (SkG), bimeron-skyrmion (BM-Sk), mixed skyrmion (MSk), vortex (VX), mixed state (MX2), noncoplanar (NCP), and AFM skyrmion crystal (AFSkX). We have taken 76 data points along the J_{AF} axis and 101 points along the h_z axis. Note that using an even finer grid of points for the parameters J_{AF} and h_z would refine the phase boundary locations and possibly could potentially reveal some tilting of the vertical phase boundaries at large J_{AF}.

AFM skyrmion crystal (AFSkX), all to be described below. In the small J_{AF} regime, the fDW state maintains its stability. As J_{AF} increases, it results in a stable SQ spiral state, which persists up to very large J_{AF} values in the presence of low magnetic fields. The fDW instability can be attributed to the lifting of degeneracies caused by the AFM term. When the J_{AF} value is increased, the exchange interaction favors long-range order, causing the system to prefer a specific spiraling plane [49].

An increase in the magnetic field results in skyrmion crystal (SkX) and skyrmion gas (SkG) states when J_{AF} is small. In the SkX state, the skyrmions form a triangular lattice, as shown in Fig. 2(a). The hexagonal arrangement of skyrmions can be interpreted as a combination of three degenerate spiral states. We also found that, within the SkX phase, increasing J_{AF} leads to a decrease in skyrmion size [49]. Typically, adjusting the strength of SO coupling relative to the bandwidth is necessary to control the size of these topological magnetic textures. Interestingly, J_{AF} emerges as an independent model parameter that can modify the antiskyrmion size, potentially having practical implications. For a range of values, J_{AF} appears to function as an additive factor to the SO coupling. Previous findings indicate that the energy of a saturated ferromagnet is lower than that of the SkG phase [48], as established by contrasting the energies from simulations with increasing and decreasing magnetic fields (h_z) at low temperatures. This suggests that the SkG phase may not represent a stable ground state phase. However, the low but finite temperature entropic preference for this phase over the FM phase implies its potential significance in real-world applications [46,48]. Because the SkG state could be identified as a metastable state at $T = 0$, we indicate the SkG-FM boundary with a dotted line.

We have revealed a pocket of the bimeron-skyrmion (BM-Sk) composite phase in the phase diagram Fig. 1. Similar results are obtained using vacancies [50,51]. The BM-Sk phase is the coexistence of bimerons and skyrmions, which leads to complex and intertwined arrangements of magnetic textures [52]. The coexistence of these textures can result in intricate patterns that deviate from simple periodic lattice structures, providing an unconventional magnetic landscape. The bimeron-skyrmion phase can exhibit distinct scalar spin chirality due to the interaction between skyrmions and bimerons [53,54].
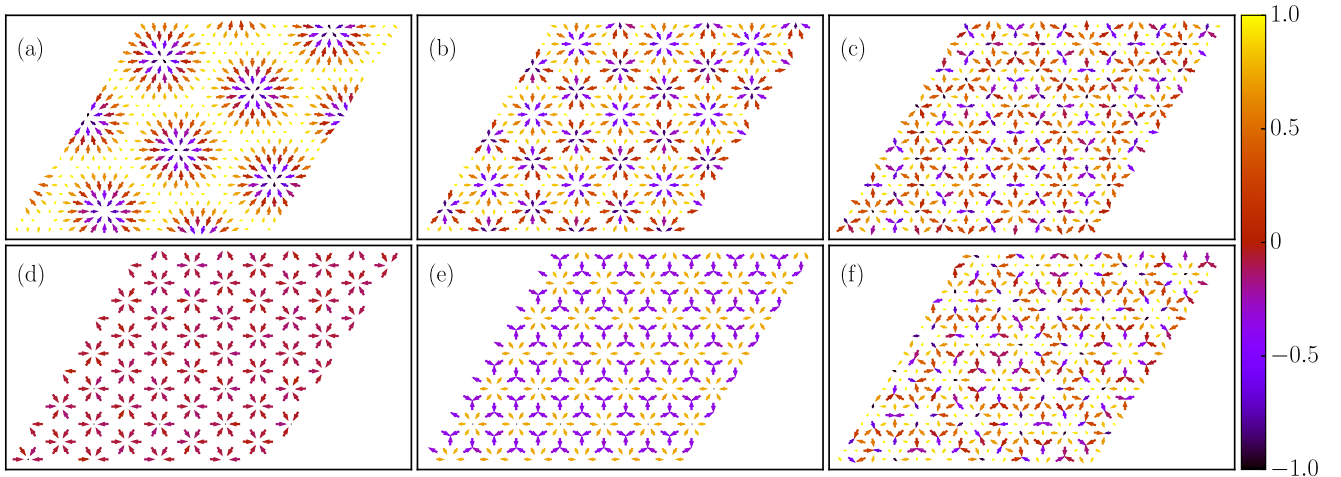
FIG. 2. Snapshots of typical spin configurations, at low temperature $T = 0.001$, representative of the many phases found in this study. In particular: (a) SkX at $J_{AF} = 0.01$, $h_z = 0.16$; (b) MSk at $J_{AF} = 0.22$, $h_z = 0.3$; (c) MX at $J_{AF} = 0.52$, $h_z = 0.57$; (d) VX at $J_{AF} = 0.31$, $h_z = 0.32$; (e) NCP at $J_{AF} = 0.64$, $h_z = 1.1$; and (f) AFSkX at $J_{AF} = 0.73$, $h_z = 1.51$. The planar components of the spin vectors are represented by the arrows, while the z component is color coded. We have displayed a 24×24 section of the 48×48 lattice used for Monte Carlo simulations.
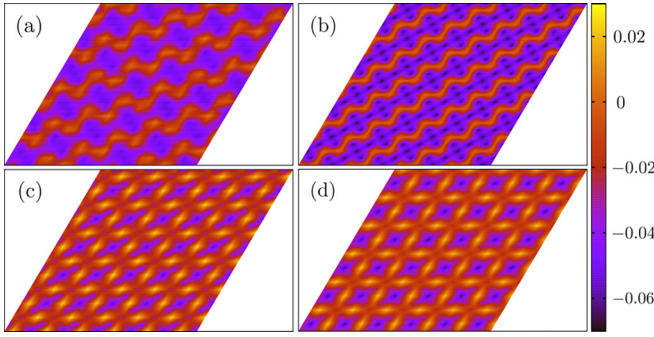
FIG. 3. Low temperature skrmion density profile for: (a) MSk at $J_{AF} = 0.22$ and $h_z = 0.3$, (b) VX at $J_{AF} = 0.31$ and $h_z = 0.32$, (c) NCP at $J_{AF} = 0.64$ and $h_z = 1.1$, and (d) AFSkX at $J_{AF} = 0.73$ and $h_z = 1.51$.

FIG. 4. Comparison of the topological Hall conductivity σ_{xy} for the unconventional magnetic phases in the phase diagram.

We observed a unique mixed skyrmion (MSk) phase in the range $0.20 < J_{AF} < 0.28$ [see Fig. 2(a)]. This phase represents the coexistence of two different skyrmions with different helicities, namely helicities 0 and $\frac{2\pi}{3}$. The profile of the local skyrmion density $\mathcal{T}_i$ for the MSk phase is shown in Fig. 3(a). The $\mathcal{T}_i$ profile exhibits diffuse diagonal strips with oscillatory positive and negative modulations. This unusual $\mathcal{T}_i$ profile is indicative of the coexistence of different types of skyrmions. A similar coexisting phase is known to exist in Heusler materials for which the current microscopic model could be relevant [55].

Increasing the exchange coupling, we find a vortex state (VX), immersed in an antiferromagnetic background, in the range $0.29 < J_{AF} < 0.34$ [see Fig. 2(d)]. This vortex state is of Néel type, with helicity 0. The skyrmion density $\mathcal{T}_i$ profile is shown in Fig. 3(b). The existence of a Néel type vortex state was also realized in the weak Kondo region [56], supporting the generality of our proposed microscopic mechanism. We believe that our findings not only provide valuable insights into the creation of the intricate noncoplanar spin configurations observed in experimental settings, such as monolayer metals on substrates [56–58], but also lay the groundwork for investigating additional unconventional spin textures in polar and chiral systems.

An exotic mixed state (MX) in a wide region $0.35 < J_{AF} < 0.61$ was found to be stable. The spin configuration [Fig. 2(c)] reveals interpenetrating skyrmion states. The MX state shows a large topological Hall response, as seen in Fig. 4. These unique overlapping skyrmion states are considered to be favorable candidates for spintronics applications because of their suppressed skyrmion Hall effect [25,41] and, consequently, are of considerable interest nowadays. At large J_{AF}, we find a noncoplanar magnetic (NCP) state in the range $0.62 < J_{AF} < 0.69$. The spin configuration [see Fig. 2(e)] shows small Néel skyrmions closely packed in the background of a 120° spin state. This NCP state possesses topological characteristics, clearly shown in Fig. 3(c). The negative skyrmion density values map the positions of Néel skyrmions. Lastly, in this rich phase diagram, we have the antiferromagnetic skyrmion crystal (AFSkX) state Fig. 2(f). The skyrmion density ($\mathcal{T}_i$) plot [Fig. 3] reveals the detailed nature of this AFM-skyrmion crystal state. To better understand the state, we also present the sublattice resolved spin configurations.
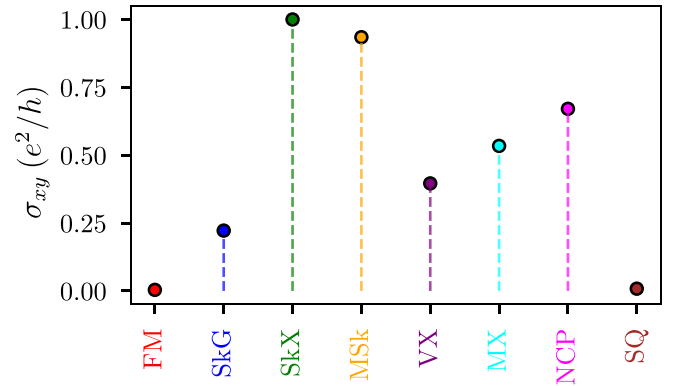
This state is a lattice superposition of three Néel skyrmions, as revealed in the sublattice resolved spin configuration plot.

IV. TOPOLOGICAL HALL EFFECT

The noncoplanar phases and chiral magnetic structures, such as skyrmions, are known for inducing a topological Hall effect, resulting from the emergent magnetic field $B_z = \frac{1}{2}\mathbf{S} \cdot (\partial_x \mathbf{S} \times \partial_y \mathbf{S})$ generated by the magnetic texture [59]. To better understand the emergent unconventional magnetic phase resulting from interfacial frustration and intrinsic Rashba SOC, we have analyzed the topological Hall response and compared it to that of the topologically trivial phases. In order to compute the transverse Hall conductivity, we consider the following canonical Kubo formula:

$$\sigma_{xy} = \frac{e^2 \hbar}{N} \sum_{\substack{m \\ m \neq n}} \frac{f(E_m) - f(E_n)}{(E_m - E_n)^2 + \Gamma^2} \text{Im}(\langle m|v_x|n\rangle \langle n|v_y|m\rangle), \quad (5)$$

where E_m represents the eigenvalue corresponding to the eigenstate $|m\rangle$, while $f(E_m)$ denotes the Fermi distribution function. The Lorentzian broadening parameter, Γ, is set to 0.01. The velocity operator in the γ direction, derived using the commutator with the Hamiltonian [Eq. (2)] of the position operator, can be expressed as $v_\gamma = \frac{i}{\hbar}[H_{RDE}, r_\gamma] = -\frac{i}{\hbar}\sum_{\langle ij \rangle}[g_{ij}^\gamma d_i^\dagger d_j - \text{H.c.}]$. For the current analysis, we performed the calculations at $T = 0.01$, using $t = 1$ and an electric filling fraction $n_e = 0.3$. As previously discussed in Refs. [48,52], the description exhibits no qualitative differences when alternative choices are considered provided the Fermi level lies within the metallic band in the double exchange limit.

In Fig. 4, we present the normalized topological Hall conductivity σ_{xy} [Eq. (5)] for the unconventional magnetic textures that are stable in the phase diagram (see Fig. 1). Clearly, σ_{xy} is nonzero for all the chiral magnetic phases stabilized by interfacial frustration in our model. Note the small but finite value of σ_{xy} for the fDW state, owing to its chiral nature. Indeed, it has been recently observed that domain wall structures possess an overall finite chirality [60,61]. As expected, the topologically trivial states, like FM and SQ, do not show any contribution to σ_{xy}. Nevertheless, it is interesting

that the MSk state shows nearly equal topological conductivity as the SkX state. Hence, this discovery could serve as a valuable "fingerprint" for identifying the presence of such unconventional states. Also, the vortex (VX), mixed (MX), and noncoplanar (NCP) states show robust topological responses due to their chirality and noncoplanarity. The emergence of the topological Hall effect in nonskyrmionic magnetic phases has become a fascinating subject of much recent debate [62–64]. Our findings support the existing theoretical and experimental observations using a unique interfacial-induced SOC approach. Our effort invites additional experimental research in this direction, centered on examining topological Hall effects originating from nonskyrmionic chiral magnetic structures. It also invites additional theoretical work addressing the neutron response of the novel phases as in Ref. [65] for a square lattice, using this type of exotic states in geometries searching for Majoranas [66], and unveiling further novel frustrated states in multilayer geometries [67].

V. CONCLUSIONS

In this work, we have presented the effects of interfacial frustration in spin-orbit coupled metallic triangular systems. The emergence of unconventional chiral magnetic states in skyrmion-based systems has become a fascinating area of recent research. We have studied the phase diagram of an effective Hamiltonian using classical Monte Carlo simulations. The rich phase diagram suggests the feasibility of realizing unconventional topological phases in triangular antiferromagnets. In other words, we have proposed a method for stabilizing magnetic phases, such as MSk and MX, by utilizing interfacial frustration in bilayer systems. The MSk state, characterized by the coexistence of two distinct skyrmion types with different helicities, is particularly intriguing. A similar coexistence state has been recently observed in Heusler materials [55], which underscores the relevance of our current study.

It is noteworthy that earlier studies on square lattices have shown the emergence of an antiferromagnetic skyrmion crystal state [49]. The stability of these phases can be attributed to the inherent interfacial frustration characteristic of the triangular lattice system. Additionally, these exotic magnetic phases display finite contributions to the topological Hall response. We also provide a comparative analysis of the topological Hall conductivity, which could facilitate the indirect detection of these magnetic states in experimental investigations. The chiral magnetic phases, including SkX, typically emerge below 100 K, as evidenced by topological Hall effect measurements, see Refs. [68–71]. However, in this proposed bilayer system, achieving unconventional chiral magnetic phases becomes feasible by tuning the exchange coupling.

For a potential material realization, we consider a layer of magnetic transition metal X, where X = Co, Cr, Fe, Mn, adsorbed onto a monolayer of transition metal dichalcogenides (MoS_2, WS_2, or WSe_2) [72,73]. Recent research indicates that at low temperatures, the ground state of Cr/MoS_2, Fe/MoS_2, and Fe/WSe_2 is a three-sublattice spiral [74,75]. By further reducing anisotropy through materials engineering, TMD-based antiferromagnetic triangular lattices, such as Fe/WSe_2, could potentially display unconventional skyrmion lattices. More-

over, we predict that Fe/MoS_2 may serve as a suitable host for investigating topological magnetic states under experimentally achievable magnetic fields.

APPENDIX A: CLASSICAL MONTE CARLO SIMULATIONS

We have investigated the magnetic properties of the effective spin Hamiltonian described in the main text using the classical Monte Carlo simulation technique, which is based on the conventional heat bath method [76]. Periodic boundary conditions were applied in both directions. In the presence of an external magnetic field, we utilize the zero field cooling (ZFC) protocol, where the temperature is initially slowly lowered from $T = 1.0$ to the lowest temperature point $T = 0.001$ at zero field strength ($h_z = 0$). At this lowest temperature $T = 0.001$, the magnetic field strength is then increased.

The annealing process is achieved by gradually decreasing the temperature parameter, starting at a sufficiently high value to observe the phase transition from the paramagnetic to the ordered state upon cooling. For specific T and h_z values, single spin update schemes are performed by proposing a new spin configuration from a set of uniformly distributed points on the surface of a unit sphere. This choice of selecting a completely new orientation for the spin reduces the system's tendency to become trapped in metastable states. The new configuration is accepted or rejected based on the standard Metropolis algorithm [77,78]. A Monte Carlo run at each h_z and T value consists of approximately $\sim 1 \times 10^5$ Monte Carlo steps (MCSs) for equilibration and twice that number for calculating the average of the required physical observables. For a detailed exploration of the parameter space (h_z and J_{AF}), we used a lattice size $N = 48 \times 48$. To rule out finite size effects, the stability of results was verified by simulating lattice sizes up to $N = 120 \times 120$ for some selected parameter values.

APPENDIX B: REAL-SPACE VIEW OF LOW-TEMPERATURE MAGNETIC PHASES

In this section, we present additional interesting magnetic phases which are stable in the phase diagram. Figure 5 displays representative real spin configurations for those
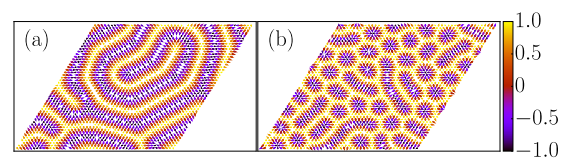
FIG. 5. Snapshots of spin configurations obtained at low temperature for (a) fDW and (b) BM-Sk states [52]. The planar components (x, y) of the spin vectors are represented by the arrows while the z component is color coded. Both for (a) and (b), we show 48×48 lattice points.

emergent magnetic states at low temperatures. The filamentary domain wall (fDW) state, as seen in Fig. 5(a), consists of a domain-wall-like structure, where the plane of spiraling can bend without incurring any energy penalty. The stability of this domain structure is attributed to an unusual degeneracy of spiral states, which emerges due to the presence of mutually orthogonal directions of the two DM vectors in our spin model [47,48]. Thermal fluctuations give rise to a metastable regime, consisting of a mixed bimeron and skyrmion (BM-Sk) phase [see Fig. 5(b)], which lies between the fDW-SkX and fDW-MSk phases.

APPENDIX C: PHYSICAL OBSERVABLES

In our classical Monte Carlo simulations, we visually identify magnetic phases at low temperatures through their corresponding real-space spin patterns. However, a quantitative measure becomes necessary in order to determine phase transitions between two phases. Consequently, we have determined the phase boundaries among various transitions through the calculation of several physical observables. Specifically, we compute the magnetic susceptibility (χ_M), topological susceptibility ($\chi_\mathcal{T}$), and chiral susceptibility ($\chi_\mathcal{L}$) [79], defined as,

$$
\begin{aligned}
\chi_M &= \frac{dM}{dh_z}, \\
\chi_\mathcal{T} &= \frac{\langle \mathcal{T}^2 \rangle - \langle \mathcal{T} \rangle^2}{NT}, \\
\chi_\mathcal{L} &= \frac{\langle \mathcal{L}^2 \rangle - \langle \mathcal{L} \rangle^2}{NT}.
\end{aligned}
\quad \text{(C1)}
$$

The angular brackets denote the Monte Carlo average of each quantity. The $\mathcal{T}$ and $\mathcal{L}$ are the local skyrmion density and local chirality, respectively [see Eq. (4) in the manuscript]. The magnetization (M) is the magnetization per site, defined as $M = \frac{1}{N} \langle \sum_i S_i^z \rangle$.

APPENDIX D: DETERMINATION OF PHASE BOUNDARIES

In our manuscript, phase boundaries presented in the phase diagram (see Fig. 1) are established through the examination of variations in magnetic susceptibility (χ_M), topological susceptibility ($\chi_\mathcal{T}$), and chiral susceptibility ($\chi_\mathcal{L}$) as a function of
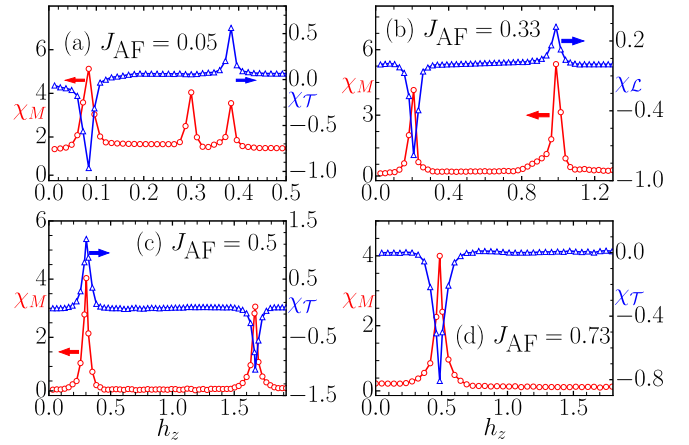
FIG. 6. Magnetic field dependence of various physical quantities for different J_{AF} values. (a), (c), (d) shows the variation of magnetic susceptibility (χ_M) [left axis, red circles] and topological susceptibility ($\chi_\mathcal{T}$) [right axis, blue triangles] at $J_{AF} = 0.05, 0.5, 0.73$. In (b), at $J_{AF} = 0.33$ in addition to χ_M [left axis, red circles], we observe similar order parameterlike behavior of the chiral susceptibility ($\chi_\mathcal{T}$) [right axis, blue triangles].

h_z. Anomalies in at least one of these quantities indicate phase boundaries.

We present data for select points in parameter space. For instance, at $J_{AF} = 0.05$ [Fig. 6(a)], distinct peaks in χ_M at $h_z = 0.085, 0.3$, and 0.384 denote phase transitions from fDW to FM via SkX and SkG. While χ_M exhibits three peaks at this parameter point, $\chi_\mathcal{T}$ reveals two, reflecting its exclusive representation of topological to nontopological transitions (fDW to SkX and SkG to FM).

At $J_{AF} = 0.33$, similar peaks in χ_M and $\chi_\mathcal{L}$ quantify the SQ to VX transition at $h_z = 0.208$ and VX to FM transition at $h_z \approx 0.988$ [Fig. 6(b)]. For moderate J_{AF}, an exotic topological MX state with interpenetrating skyrmions is observed. At $J_{AF} = 0.5$, accompanying sudden changes in $\chi_\mathcal{T}$ at $h_z = 0.3, 1.67$ [Fig. 6(c)] corroborate transitions from SQ to MX and MX to FM.

Lastly, discontinuities in χ_M and $\chi_\mathcal{T}$ at $h_z = 0.486$ [see Fig. 6(d)] signal the transition from SQ to AFSkX phases. However, it is noteworthy that finding a well-defined order parameter for disordered phases, such as fDW, SkG, and BM-Sk, is impractical. Hence, we rely on real-space spin configurations in these cases.

[1] A. Fert, N. Reyren, and V. Cros, Nat. Rev. Mater. **2**, 17031 (2017).

[2] Y. Tokura, M. Kawasaki, and N. Nagaosa, Nat. Phys. **13**, 1056 (2017).

[3] A. N. Bogdanov and C. Panagopoulos, Nat. Rev. Phys. **2**, 492 (2020).

[4] T. Jungwirth, X. Marti, P. Wadley, and J. Wunderlich, Nat. Nanotechnol. **11**, 231 (2016).

[5] N. Nagaosa and Y. Tokura, Nat. Nanotechnol. **8**, 899 (2013).

[6] A. N. Bogdanov and D. Yablonskii, Zh. Eksp. Teor. Fiz. **95**, 178 (1989).

[7] A. Bogdanov and A. Hubert, J. Magn. Magn. Mater. **138**, 255 (1994).

[8] A. N. Bogdanov, U. K. Rößler, M. Wolf, and K.-H. Müller, Phys. Rev. B **66**, 214410 (2002).

[9] A. N. Bogdanov and C. Panagopoulos, Phys. Today **73**, 44 (2020).

[10] R. Wiesendanger, Nat. Rev. Mater. **1**, 16044 (2016).

[11] A. Fert, V. Cros, and J. Sampaio, Nat. Nanotechnol. **8**, 152 (2013).

[12] K. Karube, J. S. White, D. Morikawa, C. D. Dewhurst, R. Cubitt, A. Kikkawa, X. Yu, Y. Tokunaga, T.-H. Arima, H. M. Rønnow *et al.*, Sci. Adv. **4**, eaar7043 (2018).

[13] S. Seki, X. Yu, S. Ishiwata, and Y. Tokura, Science **336**, 198 (2012).

[14] T. Adams, A. Chacon, M. Wagner, A. Bauer, G. Brandl, B. Pedersen, H. Berger, P. Lemmens, and C. Pfleiderer, Phys. Rev. Lett. **108**, 237204 (2012).

[15] T. Kurumaji, T. Nakajima, V. Ukleev, A. Feoktystov, T.-H. Arima, K. Kakurai, and Y. Tokura, Phys. Rev. Lett. **119**, 237201 (2017).

[16] S. Bordács, A. Butykai, B. G. Szigeti, J. S. White, R. Cubitt, A. O. Leonov, S. Widmann, D. Ehlers, H.-A. K. von Nidda, V. Tsurkan, A. Loidl, and I. Kézsmárki, Sci. Rep. **7**, 7584 (2017).

[17] S. Banerjee, J. Rowland, O. Erten, and M. Randeria, Phys. Rev. X **4**, 031045 (2014).

[18] W. Pan, J. L. Reno, and A. Reyes, Sci. Rep. **10**, 1 (2020).

[19] C. Wang, H. Du, X. Zhao, C. Jin, M. Tian, Y. Zhang, and R. Che, Nano Lett. **17**, 2921 (2017).

[20] S.-G. Je, H.-S. Han, S. K. Kim, S. A. Montoya, W. Chao, I.-S. Hong, E. E. Fullerton, K.-S. Lee, K.-J. Lee, M.-Y. Im *et al.*, ACS Nano **14**, 3251 (2020).

[21] D. Cortés-Ortuño, W. Wang, M. Beg, R. A. Pepper, M.-A. Bisotti, R. Carey, M. Vousden, T. Kluyver, O. Hovorka, and H. Fangohr, Sci. Rep. **7**, 4060 (2017).

[22] S. Hayami, Phys. Rev. B **103**, 224418 (2021).

[23] T. Kurumaji, T. Nakajima, M. Hirschberger, A. Kikkawa, Y. Yamasaki, H. Sagayama, H. Nakao, Y. Taguchi, T.-H. Arima, and Y. Tokura, Science **365**, 914 (2019).

[24] S. Wang, Q. Zeng, D. Liu, H. Zhang, L. Ma, G. Xu, Y. Liang, Z. Zhang, H. Wu, R. Che *et al.*, ACS Appl. Mater. Interfaces **12**, 24125 (2020).

[25] D. Toscano, J. Mendonça, A. Miranda, C. de Araujo, F. Sato, P. Coura, and S. Leonel, J. Magn. Magn. Mater. **504**, 166655 (2020).

[26] B. Göbel, A. Mook, J. Henk, and I. Mertig, Phys. Rev. B **99**, 020405(R) (2019).

[27] C. A. Akosa, H. Li, G. Tatara, and O. A. Tretiakov, Phys. Rev. Appl. **12**, 054032 (2019).

[28] N. Mukai and A. O. Leonov, Phys. Rev. B **106**, 224428 (2022).

[29] L. Shen, J. Xia, G. Zhao, X. Zhang, M. Ezawa, O. A. Tretiakov, X. Liu, and Y. Zhou, Phys. Rev. B **98**, 134448 (2018).

[30] K. Litzius, I. Lemesh, B. Krüger, P. Bassirian, L. Caretta, K. Richter, F. Büttner, K. Sato, O. A. Tretiakov, J. Förster *et al.*, Nat. Phys. **13**, 170 (2017).

[31] J. Barker and O. A. Tretiakov, Phys. Rev. Lett. **116**, 147203 (2016).

[32] S. Gao, H. D. Rosales, F. A. G. Albarracín, V. Tsurkan, G. Kaur, T. Fennell, P. Steffens, M. Boehm, P. Čermák, A. Schneidewind *et al.*, Nature (London) **586**, 37 (2020).

[33] T. Dohi, S. DuttaGupta, S. Fukami, and H. Ohno, Nat. Commun. **10**, 5153 (2019).

[34] C. A. Akosa, O. A. Tretiakov, G. Tatara, and A. Manchon, Phys. Rev. Lett. **121**, 097204 (2018).

[35] H. D. Rosales, D. C. Cabra, and P. Pujol, Phys. Rev. B **92**, 214439 (2015).

[36] P. F. Bessarab, D. Yudin, D. R. Gulevich, P. Wadley, M. Titov, and O. A. Tretiakov, Phys. Rev. B **99**, 140411(R) (2019).

[37] X. Liang, J. Xia, X. Zhang, M. Ezawa, O. A. Tretiakov, X. Liu, L. Qiu, G. Zhao, and Y. Zhou, Appl. Phys. Lett. **119**, 062403 (2021).

[38] A. Mukherjee, D. S. Kathyat, and S. Kumar, Phys. Rev. B **103**, 134424 (2021).

[39] A. Mukherjee, D. S. Kathyat, and S. Kumar, Sci. Rep. **11**, 9566 (2021).

[40] Q. Shao, Y. Liu, G. Yu, S. K. Kim, X. Che, C. Tang, Q. L. He, Y. Tserkovnyak, J. Shi, and K. L. Wang, Nat. Electron. **2**, 182 (2019).

[41] X. Zhang, Y. Zhou, and M. Ezawa, Nat. Commun. **7**, 10293 (2016).

[42] A. S. Ahmed, A. J. Lee, N. Bagués, B. A. McCullian, A. M. Thabt, A. Perrine, P.-K. Wu, J. R. Rowland, M. Randeria, P. C. Hammel *et al.*, Nano Lett. **19**, 5683 (2019).

[43] Y. Cheng, S. Yu, M. Zhu, J. Hwang, and F. Yang, Phys. Rev. Lett. **123**, 237206 (2019).

[44] P. Zhang, J. Finley, T. Safi, and L. Liu, Phys. Rev. Lett. **123**, 247206 (2019).

[45] B. Göbel, A. Mook, J. Henk, and I. Mertig, Phys. Rev. B **96**, 060406(R) (2017).

[46] D. S. Kathyat, A. Mukherjee, and S. Kumar, Phys. Rev. B **104**, 184434 (2021).

[47] D. S. Kathyat, A. Mukherjee, and S. Kumar, Phys. Rev. B **102**, 075106 (2020).

[48] D. S. Kathyat, A. Mukherjee, and S. Kumar, Phys. Rev. B **103**, 035111 (2021).

[49] A. Mukherjee, D. S. Kathyat, and S. Kumar, Phys. Rev. B **105**, 075102 (2022).

[50] R. L. Silva, L. D. Secchin, W. A. Moura-Melo, A. R. Pereira, and R. L. Stamps, Phys. Rev. B **89**, 054434 (2014).

[51] V. Esposito, X. Zheng, M. Seaberg, S. Montoya, B. Holladay, A. Reid, R. Streubel, J. Lee, L. Shen, J. Koralek *et al.*, Appl. Phys. Lett. **116**, 181901 (2020).

[52] N. Mohanta, E. Dagotto, and S. Okamoto, Phys. Rev. B **100**, 064429 (2019).

[53] S. K. Kim, Phys. Rev. B **99**, 224406 (2019).

[54] W. Sun, W. Wang, H. Li, G. Zhang, D. Chen, J. Wang, and Z. Cheng, Nat. Commun. **11**, 5930 (2020).

[55] D. Shimizu, T. Nagase, Y.-G. So, M. Kuwahara, N. Ikarashi, and M. Nagao, arXiv:2008.07272.

[56] S. Hayami and Y. Motome, Phys. Rev. Lett. **121**, 137202 (2018).

[57] S. Heinze, K. Von Bergmann, M. Menzel, J. Brede, A. Kubetzka, R. Wiesendanger, G. Bihlmayer, and S. Blügel, Nat. Phys. **7**, 713 (2011).

[58] B. Zimmermann, M. Heide, G. Bihlmayer, and S. Blügel, Phys. Rev. B **90**, 115427 (2014).

[59] T. Schulz, R. Ritz, A. Bauer, M. Halder, M. Wagner, C. Franz, C. Pfleiderer, K. Everschor, M. Garst, and A. Rosch, Nat. Phys. **8**, 301 (2012).

[60] S. K. Karna, M. Marshall, W. Xie, L. DeBeer-Schmitt, D. P. Young, I. Vekhter, W. A. Shelton, A. Kovács, M. Charilaou, and J. F. DiTusa, Nano Lett. **21**, 1205 (2021).

[61] P. Schoenherr, J. Müller, L. Köhler, A. Rosch, N. Kanazawa, Y. Tokura, M. Garst, and D. Meier, Nat. Phys. **14**, 465 (2018).

[62] J. J. Nakane, K. Nakazawa, and H. Kohno, Phys. Rev. B **101**, 174432 (2020).

[63] P. K. Rout, P. V. P. Madduri, S. K. Manna, and A. K. Nayak, Phys. Rev. B **99**, 094430 (2019).

[64] J. H. Jeon, H. R. Na, H. Kim, S. Lee, S. Song, J. Kim, S. Park, J. Kim, H. Noh, G. Kim *et al.*, ACS Nano **16**, 8974 (2022).

[65] N. Mohanta, A. D. Christianson, S. Okamoto, and E. Dagotto, Commun. Phys. **3**, 229 (2020).

[66] N. Mohanta, S. Okamoto, and E. Dagotto, Commun. Phys. **4**, 163 (2021).

[67] N. Mohanta and E. Dagotto, npj Quantum Mater. **7**, 76 (2022).

[68] A. Neubauer, C. Pfleiderer, B. Binz, A. Rosch, R. Ritz, P. G. Niklowitz, and P. Böni, Phys. Rev. Lett. **102**, 186602 (2009).

[69] J. Matsuno, N. Ogawa, K. Yasuda, F. Kagawa, W. Koshibae, N. Nagaosa, Y. Tokura, and M. Kawasaki, Sci. Adv. **2**, e1600304 (2016).

[70] L. Wang, Q. Feng, Y. Kim, R. Kim, K. H. Lee, S. D. Pollard, Y. J. Shin, H. Zhou, W. Peng, D. Lee *et al.*, Nat. Mater. **17**, 1087 (2018).

[71] L. Vistoli, W. Wang, A. Sander, Q. Zhu, B. Casals, R. Cichelero, A. Barthélémy, S. Fusil, G. Herranz, S. Valencia *et al.*, Nat. Phys. **15**, 67 (2019).

[72] A. Allain, J. Kang, K. Banerjee, and A. Kis, Nat. Mater. **14**, 1195 (2015).

[73] W. Zhang, P. K. J. Wong, X. Zhou, A. Rath, Z. Huang, H. Wang, S. A. Morton, J. Yuan, L. Zhang, R. Chua *et al.*, ACS Nano **13**, 2253 (2019).

[74] D. W. Latzke, W. Zhang, A. Suslu, T.-R. Chang, H. Lin, H.-T. Jeng, S. Tongay, J. Wu, A. Bansil, and A. Lanzara, Phys. Rev. B **91**, 235202 (2015).

[75] W. Fang, A. Raeliarijaona, P.-H. Chang, A. A. Kovalev, and K. D. Belashchenko, Phys. Rev. Mater. **5**, 054401 (2021).

[76] K. Binder, D. Heermann, L. Roelofs, A. J. Mallinckrodt, and S. McKay, Comput. Phys. **7**, 156 (1993).

[77] N. Metropolis, A. W. Rosenbluth, M. N. Rosenbluth, A. H. Teller, and E. Teller, J. Chem. Phys. **21**, 1087 (1953).

[78] W. K. Hastings, Biometrika **57**, 97 (1970).

[79] D. Amoroso, P. Barone, and S. Picozzi, Nat. Commun. **11**, 5784 (2020).